Testing the ion-current model for flagellar length sensing and IFT regulation

Hiroaki Ishikawa[1], Jeremy Moore[2,†], Dennis R. Diener[3], Markus Delling[4], Wallace F. Marshall[1*]

1. Department of Biochemistry and Biophysics, University of California San Francisco, San Francisco, CA 94143
2. Kenyon College, Gambier, OH, 43022 and Summer Research Training Program at University of California San Francisco, San Francisco, CA 94143
3. Max Planck Institute of Molecular Cell Biology and Genetics, Dresden, Germany 01307
4. Department of Physiology, University of California San Francisco, San Francisco, CA 94143

*Corresponding authors: Wallace F. Marshall
Address: UCSF Mail Code 2200
Genentech Hall Room N372F
600 16th St.
San Francisco, CA 94143
Phone: (415) 514-4304
Fax: (415) 502-4315
Email: wallace.marshall@ucsf.edu

† Present address
Department of Molecular Cellular and Developmental Biology, Yale University, New Heaven, CT 06511

Keywords
Cilia, flagella, intraflagellar transport, calcium

Abstract

Eukaryotic cilia and flagella are microtubule-based organelles whose relatively simple shape makes them ideal for investigating the mechanisms of fundamental size regulation. Most of the flagellar materials are transported from the cell body via an active transport process called intraflagellar transport (IFT) because no protein synthesis occurs in the flagellum. The rate of IFT injection has been shown to negatively correlate with flagellar length. However, it remains unknown how the cell measures the length of its flagella and controls IFT injection. One of the most-discussed theoretical models for length sensing to control IFT is the ion-current model, which posits that there is a uniform distribution of Ca^{2+} channels along the flagellum and that the Ca^{2+} current from the flagellum into the cell body increases linearly with flagellar length. In this model, the cell uses the Ca^{2+} current to negatively regulate IFT injection. The recent discovery that IFT entry into flagella is regulated by a CDPK has provided further impetus for the ion current model. To test this model, we measured and manipulated the levels of Ca^{2+} inside of *Chlamydomonas* flagella and quantified IFT injection. Although the concentration of Ca^{2+} inside of flagella was weakly correlated with the length of flagella, we found that IFT injection was reduced in calcium-deficient flagella, rather than increased as the model predicted, and that variation in IFT injection was uncorrelated with the occurrence of flagellar Ca^{2+} spikes. Thus, Ca^{2+} does not work as a negative regulator of IFT injection, hence it cannot form the basis of a stable length control system.

Introduction

The mechanism by which cells control the size of organelles is a fundamental question in cell biology. Cells control the size of their organelles to efficiently use their energy and space (Chan and Marshall, 2012). However, it is mostly unknown how cells regulate organelle size, in part because the complexity of many organelles makes their size control mechanisms difficult to study. Eukaryotic cilia and flagella (we use these terms interchangeably) are an ideal model system to study size regulation because they consist of a simple, hair-like structure that can change in length while maintaining a constant diameter. Cilia and flagella are microtubule-based organelles that protrude from the cell body and are important for sensing extracellular signals and producing fluid flows (Ishikawa and Marshall, 2011; Reiter and Leroux, 2017). It is known that the length of cilia and flagella is cell type specific. For example, the biflagellate green alga *Chlamydomonas reinhardtii* adjusts the length of both flagella to a length suitable for swimming (Bauer et al., 2021; Bottier et al., 2019). If the flagella are too long or too short, the cells cannot swim efficiently. When flagella are removed from a cell, new flagella regenerate to the pre-severing length in around 90 min (Rosenbaum et al., 1969). Flagellar growth slows before they become full-length. This decelerating growth rate suggests that there is some mechanism that regulates the growth rate as a function of length.

Assembly and maintenance of flagella are dependent on an active transport system, intraflagellar transport (IFT). Because no protein synthesis occurs in the flagellum, new materials must be injected into the flagellum by a process called IFT injection. IFT is mediated by huge protein complexes called trains, which have an elongate shape and move on the flagellar axoneme back and forth like a train (Jordan et al., 2018; Pigino et al., 2009). IFT trains are carried to the flagellar tip by a heterotrimeric kinesin-2 motor and returned to the cell body by cytoplasmic dynein 2 (Ishikawa and Marshall, 2011; Rosenbaum and Witman, 2002). It is known that the rate of IFT injection is negatively correlated with the length of flagella during the regeneration of cilia (Engel et al., 2009; Ludington et al., 2013), but it is unknown how cells regulate the rate of IFT

81 injection. To explain this negative correlation, several theoretical models have been
82 proposed (Chan and Marshall, 2012; Ludington et al., 2015; Rosenbaum, 2003).
83 One well-known model for the regulation of IFT injection, which we term the ion-
84 current model (also known as ciliary-current model) was first proposed by Rosenbaum
85 (2003) based on a previous electrophysiological study showing that voltage-gated
86 calcium channels were present in flagella at constant density (Beck and Uhl, 1994), such
87 that the number of voltage-gated calcium channels in the flagellum increases as the
88 flagellum elongates. Changes in flagellar calcium concentrations, due to changes in the
89 number and activity of calcium channels in the elongating flagella, were proposed to affect
90 calcium-dependent signaling pathways to regulate the rate of IFT injection or microtubule
91 assembly (Rosenbaum, 2003). In fact, changes in external Ca^{2+} are known to change
92 flagella length in *Chlamydomonas* (Lefebvre et al., 1978; Quader et al., 1978; Tuxhorn et
93 al., 1998). The calcium ion-current model was first proposed based on physiological
94 measurements, but at the time, the molecular identity of the voltage-gated calcium
95 channel in the flagellar membrane was not known. More recently, several calcium channel
96 proteins have been shown to localize on the *Chlamydomonas* flagellum (Fujiu et al., 2011,
97 2009; Huang et al., 2007; Pazour et al., 2005). CAV2 is a subunit of a voltage-gated
98 calcium channel which resides in the flagellar membrane (Fujiu et al., 2009). The *ppr2*
99 mutant has a mutation in the CAV2 gene and is defective in the photophobic response
100 (Fujiu et al., 2009; Matsuda et al., 1998). TRP channels are also found in *Chlamydomonas*
101 flagella (Fujiu et al., 2011; Huang et al., 2007).
102 In the original ion-current model, it was not specified how Ca^{2+} contributes to
103 flagellar length regulation, but a potential molecular mechanism has been proposed by
104 Pan and colleagues (Liang et al., 2014, 2018), who found that a subunit of heterotrimeric
105 kinesin that drives IFT anterograde motion, FLA8/KIF3B, is phosphorylated by a calcium-
106 dependent protein kinase, CDPK1, and this phosphorylation negatively regulates IFT
107 injection into flagella. Because this work provides a potential missing link in understanding
108 the ion current model, calcium-mediated regulation of IFT entry has increasingly been
109 viewed as a likely means of regulating IFT in response to flagellar length (Engelke et al.,
110 2019; Jiang et al., 2019; Kumari and Ray, 2022; Lechtreck et al., 2017; Liang et al., 2018).

111 There is thus a pressing need to test whether this model does in fact account for IFT
112 regulation as a function of length. The ion-current model hinges on two critical
113 assumptions (Figure 1A), both of which are experimentally testable. First, the amount of
114 flagellar Ca^{2+} needs to be an increasing function of the flagellar length. This would allow
115 Ca^{2+} to serve as a length indicator within the ion-current model. Second, for the ion-
116 current model to work, cellular Ca^{2+} must negatively regulate IFT injection or assembly of
117 the axoneme. This is because if the amount of flagellar Ca^{2+} increases with the flagellar
118 length, it must work as a negative regulator to control the length of flagella in order to
119 have a stable length control system with negative feedback. If Ca^{2+} positively regulates
120 IFT injection, it could not be part of a stable feedback control loop and would instead
121 produce positive feedback.
122 Here, we tested the two underlying assumptions of the ion-current model by
123 quantitatively measuring the Ca^{2+} concentration inside of *Chlamydomonas* flagella using
124 a genetically encoded calcium indicator and IFT injection in wild-type and calcium-
125 deficient flagella. The amount of Ca^{2+} inside of flagella was indeed correlated with the
126 length of flagella, as the model requires. However, IFT injection was reduced in calcium-
127 deficient flagella, rather than increased as a model predicted. We then examined
128 fluctuations of IFT at the time scale of individual injection events and compared these
129 fluctuations to fluctuations in flagellar Ca^{2+}, and found no correlation, again suggesting
130 that flagellar Ca^{2+} does not regulate IFT injection. Thus, flagellar Ca^{2+} apparently does
131 not work as a negative regulator of IFT injection and therefore could not form the basis of
132 a stable length control system. These observations are thus inconsistent with the ion-
133 current model.
134

Results

Model for the ion-current model using kinesin phosphorylation

Before testing the calcium-based model experimentally, we first asked whether it could provide a stable length control mechanism, even in theory. We constructed a simplified model for flagellar length dynamics assuming that calcium entry is proportional to flagellar length and that kinesin-2 activity is regulated by phosphorylation mediated by CDPK1 as previously reported (Liang et al., 2014) and summarized in Figure 1B. Details of this model, which integrates IFT mediated transport, Ca^{2+} influx, and CDPK activity modulating IFT entry, are provided in Materials and Methods. As shown in Figure 1C, this model is able to produce a stable length control system, such that when flagella are removed they grow back to the correct length with decelerating kinetics that resemble those seen in actual flagella. Figure 1D further shows that the relative level of phosphorylation of kinesin changes during regeneration, smoothly increasing as the length increases, consistent with the experimental observations reported by Liang et al (2014). We note that this is a highly simplified model, and detailed numerical comparison to experiments is not useful since a number of parameters have unknown values. Nevertheless, this model serves to confirm the intuition that Ca^{2+} influx proportional to flagellar length, combined with CDPK-mediated regulation of IFT injection could, at least in principle, provide a length control mechanism.

Quantitative flagellar Ca^{2+} detection using GCaMP

The first assumption of the ion-current model that we explore is the requirement that Ca^{2+} amount in the flagellum should be an increasing function of flagellar length. To measure the amount of Ca^{2+} in *Chlamydomonas* flagella, we constructed *Chlamydomonas* strains which express GCaMP, a genetically encoded calcium indicator (Nakai et al., 2001), anchored in its flagella. GCaMP was fused to the C-terminus of dynein regulatory complex 4 (DRC4), an axonemal protein (Rupp and Porter, 2003), and DRC4-GCaMP was expressed in the *pf2-4* mutant cells, a loss-of-function mutant of DRC4. DRC4-GCaMP was localized along the length of flagella (Figure 2A) and rescued the defective flagellar

165 motility phenotype of the *pf2-4* mutant. DRC4 is a component of the Nexin-Dynein
166 Regulatory Complex, which is a part of the 96-nm axonemal repeat, periodical structures
167 on the axoneme (Heuser et al., 2009; Rupp and Porter, 2003). Therefore, the amount of
168 DRC4-GCaMP is constant per unit length, and the total quantity of DRC4-GCaMP
169 associated with axonemes is determined solely by the length of the flagella. We
170 previously showed that the amount of several different axonemal proteins, such as FAP20
171 and RSP3, is constant per unit length using GFP (Ishikawa et al., 2022). This result means
172 that our system using DRC4-GCaMP should be able to quantitatively detect flagellar Ca^{2+}.
173 To confirm that axonemal DRC4-GCaMP produces a signal that depends
174 quantitatively on free Ca^{2+}, we measured the GCaMP intensity using isolated DRC4-
175 GCaMP axonemes. We isolated flagella from DRC4-GCaMP (or DRC4-mCherry-
176 GCaMP) cells and removed the membrane from flagella so that Ca^{2+} can access the
177 axoneme-associated DRC4-GCaMP (or DRC4-mCherry-GCaMP). Isolated axonemes
178 were observed in various concentrations of free Ca^{2+} solutions (Figure 2B) and the
179 intensity was quantified (Figure 2C). GCaMP fluorescence showed a sigmoidal curve with
180 respect to free Ca^{2+} concentration, with an approximately linear response in the range of
181 free Ca^{2+} from 0.05 to 1 μM. Figure 2C provides a calibration curve that lets us
182 quantitatively measure Ca^{2+} in *Chlamydomonas* flagella based on DRC4-GCaMP
183 fluorescence.
184
185 **The Ca^{2+} influx into the flagellum is correlated with flagellar length**
186 To check whether the amount of Ca^{2+} influx into the flagellum is increased with increasing
187 flagellar length, we observed DRC4-GCaMP in flagella of living cells using total internal
188 reflection fluorescence (TIRF) microscopy during flagellar regeneration. *Chlamydomonas*
189 flagella were amputated with the pH shock method (see Materials and Methods), allowing
190 us to measure Ca^{2+} influx as a function of flagellar length as the flagella regrow. We
191 observed intensity fluctuation of GCaMP in live cells indicating the presence of Ca^{2+} influx
192 (Figure 3A and Movie S1). This intensity fluctuation was not observed when 1 mM EGTA
193 was added to the media (~150 nM of free Ca^{2+}, which is the same level as the cytosolic

194 Ca^{2+} concentration, Figure 3A and Movie S3). This result indicated that most of the Ca^{2+}
195 influx came from outside of the cell.
196 TIRF movies of DRC4-GCaMP were converted into kymographs to measure the
197 calcium amount in the flagellum (Figure 3A). The amount of flagellar Ca^{2+} influx was
198 significantly correlated with the flagellar length, but with a broad distribution of values
199 around the trend line (Figure 3B, Pearson correlation coefficient $\rho = 0.33$, and coefficient
200 of determination $r^2 = 0.11$). Longer flagella generally allowed more Ca^{2+} influx but also
201 had greater variability. This variability is mainly caused by the fact that the Ca^{2+} influx
202 does not occur consistently. The frequency of flagellar Ca^{2+} influx events (spikes) was not
203 correlated with the flagellar length (Figure 3C, $\rho = 0.14$, and $r^2 = 0.02$). The pattern of
204 Ca^{2+} influx events varied from flagellum to flagellum and from time to time and did not
205 match a Poisson distribution (Figures S1 and S2). Consistent with previous reports, the
206 Ca^{2+} influx of the flagellum was compartmentalized, such that there was no correlation in
207 Ca^{2+} influx events between the two flagella from the same cell (Figures 3A, S1, and Movie
208 S1) (Collingridge et al., 2013).
209 To reduce the Ca^{2+} influx into the flagellum, we used a calcium channel mutant
210 strain, *ppr2* (Fujiu et al., 2009; Matsuda et al., 1998). The *ppr2* mutant has an insertion in
211 the CAV2 gene, which encodes a voltage-gated calcium channel localized to flagella
212 (Fujiu et al., 2009). In the *ppr2* mutant, we still observed Ca^{2+} influx events, but the amount
213 of Ca^{2+} influx was no longer correlated with the flagellar length (Figure 3B, $\rho = 0.09$, and
214 $r^2 = 0.02$) and the magnitude of influx was smaller than control on the average (Figure
215 3D). Interestingly, the *ppr2* mutant reduced Ca^{2+} influx most strongly at the distal region
216 of flagella (Figure 3A). This reduction is presumably caused by the loss of CAV2 protein,
217 which localizes the distal part of the flagellum (Fujiu et al., 2009).
218
219 **IFT injection was reduced in calcium-deficient flagella**
220 As discussed above, in order for the ion-current model to work, Ca^{2+} would need to be a
221 negative regulator of IFT injection. Any reduction in Ca^{2+} influx should thus lead to
222 increased IFT injection. Because the amount of Ca^{2+} influx into flagella was reduced in
223 the *ppr2* mutant (Figures 3 B and D), IFT injection in the *ppr2* mutant should be increased

224 compared to control cells if the ion-current model is correct. To test this prediction, we
225 quantified the IFT injection using kinesin-associated protein (KAP), which is a subunit of
226 the heteromeric kinesin-2 motor (IFT kinesin), tagged with a green fluorescent protein
227 (GFP). We focused on the kinesin-2 motor because this is the component of IFT that is
228 apparently regulated by Ca^{2+} (Liang et al., 2018, 2014). KAP-GFP was expressed in the
229 *fla3* mutant, which has a point mutation in the *FLA3* gene (encodes KAP), and rescues
230 the phenotype of the *fla3* mutant (Mueller et al., 2005). This *fla3* KAP-GFP strain was also
231 used in previous studies for measuring IFT injection intensity (Engel et al., 2009; Ishikawa
232 and Marshall, 2017; Ludington et al., 2013). Movies of KAP-GFP were converted into
233 kymographs to measure IFT injection (Figure 4A and Movies S4-S6). Similar to previous
234 reports (Ishikawa and Marshall, 2017; Ludington et al., 2013), injection intensity of KAP-
235 GFP decreases as flagellar length increases in control cells (Figure 4B). In the *ppr2*
236 mutant, IFT injection was also negatively correlated with the flagellar length but was
237 reduced in short flagella compared to control cells (Figure 4B). This is the opposite of the
238 prediction of the ion-current model. To confirm that flagellar Ca^{2+} is related to this IFT
239 reduction phenotype, we treated wild-type cells with 1 mM EGTA and measured the
240 intensity of IFT injection. EGTA treated cells showed reduced, rather than increased, IFT
241 injection, similar to that seen in *ppr2* mutant cells (Figure 4B). Because reduction in Ca^{2+}
242 caused a decrease, rather than an increase in IFT injection, these results suggested that
243 flagellar Ca^{2+} does not work as a negative regulator of IFT injection. Our observations
244 thus do not support the ion-current model.
245
246 **Effect of Ca^{2+} on flagellar regeneration and disassembly**
247 The preceding results were based on quantifying KAP entry into flagella. As an alternative
248 indicator of IFT based on IFT function, we note that IFT is thought to drive flagellar
249 elongation, such that increased IFT injection should lead to faster flagellar growth, while
250 decreased IFT injection should lead to slower growth. Flagellar growth can thus be used
251 as an indicator of functionally altered IFT injection. To confirm our result that flagellar Ca^{2+}
252 does not inhibit IFT injection as predicted by the ion-current model, we performed flagellar
253 regeneration assays while altering Ca^{2+} concentrations. *Chlamydomonas* cells were

254 treated with low-pH media to remove their flagella and cultured with TAP media with or
255 without 1 mM EGTA (free Ca^{2+} in the two types of media is 149.3 nM and 170 μM,
256 respectively). 150 nM free Ca^{2+} is comparable to the cytosolic Ca^{2+} concentration but was
257 enough to eliminate detectable flagellar Ca^{2+} influx (Figure 3A and Movie S3). 1 mM
258 EGTA treated cells showed slower flagellar regeneration than control cells but could
259 eventually reach the original length of flagella (Figure 5A, orange triangles). This
260 observation is consistent with previous studies (Liang and Pan, 2013) but is contrary to
261 the prediction of the ion-current model, in which reduction of calcium should lead to faster
262 regeneration due to increased IFT injection.

263 These findings suggested that at least a cytoplasmic concentration of Ca^{2+} is
264 enough for flagellar regeneration, and further Ca^{2+} influx into the flagellum is not essential.
265 Interestingly, the *ppr2* mutant cells showed slower flagellar regeneration and shorter final
266 length than 1 mM EGTA treated cells even though the *ppr2* mutants still have some Ca^{2+}
267 influx events (Figure 5A, red square). In any case, Ca^{2+} influx through CAV2 is apparently
268 not necessary for assembly of flagella, and CAV2 might have another role for flagellar
269 assembly or maintenance. To investigate whether extracellular Ca^{2+} can promote flagellar
270 assembly, we added 1 mM $CaCl_2$ to TAP media after pH shock. Flagellar regeneration
271 kinetics in $CaCl_2$ added media did not change relative to normal TAP media (Figure 5A,
272 green diamonds). The extra amount of extracellular Ca^{2+} does not help assembly of
273 flagella, again contrary to the ion-current model.

274 While flagellar Ca^{2+} does not seem to affect either IFT injection or flagellar
275 assembly in the way expected from the ion channel model, an alternative would be that
276 flagellar Ca^{2+} might promote flagellar disassembly, such that longer flagella would
277 experience a faster disassembly rate. We therefore tested how flagellar Ca^{2+} affects
278 flagellar disassembly using the temperature-sensitive *fla10* mutant cells (Huang et al.,
279 1977). The *fla10* mutant cells gradually reduce their flagellar length at the restrictive
280 temperature (Huang et al., 1977; Marshall et al., 2005). The *ppr2* mutation had no clear
281 effect on disassembly rates, and EGTA treated cells showed faster disassembly kinetics
282 than untreated cells in both control and *ppr2* mutant cells (Figure 5B), rather than the
283 slower kinetics that would be predicted if flagellar Ca^{2+} normally promoted disassembly.

284 Overall, our results suggest that flagellar Ca^{2+} does not inhibit IFT injection or flagellar
285 assembly or promote flagellar disassembly.
286
287 **Flagellar Ca^{2+} does not change IFT injection even at short timescales**
288 Our analyses suggested that flagellar Ca^{2+} helps flagellar assembly and maintenance
289 rather than flagellar disassembly and does not inhibit IFT injection. However, this
290 conclusion is based on separate measurements of Ca^{2+} and IFT and a comparison of
291 population averages as a function of length, leaving open the possibility that there could
292 be correlations between Ca^{2+} influx and IFT injection over short periods of time. Such a
293 short time scale correlation might be important given that calcium shows spiking dynamics
294 and could play a role in reducing flagellar length fluctuations. To ask how flagellar Ca^{2+}
295 might contribute to flagellar length control or IFT injection over short time scales in
296 individual flagella, we performed dual-channel live-cell imaging of Ca^{2+} and IFT using
297 DRC4-GCaMP and mScarlet-IFT54 (Figure 6A and Movie S7). IFT injection measured in
298 dual-channel imaging was negatively correlated with flagellar length, similar to our KAP-
299 GFP analysis (Figure 6B). Both frequency and speed of anterograde mScarlet-IFT54
300 showed a similar distribution with KAP-GFP (Figures 4C, 4D, 6C, and 6D). Likewise,
301 GCaMP intensity measured in dual-channel imaging also showed a similar distribution as
302 previously seen in our single-wavelength imaging (Figure 6E). However, there was no
303 obvious correlation between Ca^{2+} influx and IFT injection (Figure 6F), consistent with our
304 results above comparing separate single-channel imaging data.
305 To further investigate the potential effect of Ca^{2+} influx on IFT behavior on a short
306 time scale, we asked whether a burst of Ca^{2+} influx might cause a transient change in IFT
307 behavior. We selected kymograph regions in which there was no observed Ca^{2+} influx for
308 at least 10 s before a Ca^{2+} burst and analyzed successive 5 s intervals (Figure 7A). In
309 this analysis, we did not find a statistically significant difference in intensity or frequency
310 of IFT injection during the time windows before or after Ca^{2+} influx (Figure 7 B and C).
311 However, both anterograde and retrograde IFT speeds appeared to increase during Ca^{2+}
312 influx. In fact, most IFT trains did not show altered speed. The increase in average speed
313 was caused by the fact that paused IFT trains, which had an initial speed of zero, became

314 re-activated during the Ca^{2+} bursts, consistent with a previous report (Collingridge et al.,
315 2013; Fort et al., 2021). In experiments in which cells were treated with 1 mM EGTA, a
316 slowdown of IFT trains was also observed (Figure 4D). Moreover, the background
317 intensity of the mScarlet-IFT54 channel decreased after Ca^{2+} influx. This means that IFT
318 trains, which paused and accumulated during prolonged absence of Ca^{2+} influx, restarted
319 with Ca^{2+} influx. Because most of the pausing IFT trains were retrograde IFT, the intensity
320 of the returning IFT was increased after Ca^{2+} influx (Figure 7C). This result showed that
321 Ca^{2+} bursts can clear out the accumulated retrograde IFT trains from flagella. Because a
322 portion of IFT trains, after returning to the base, can be reused as new anterograde IFT
323 trains (Wingfield et al., 2017), we expected that IFT injection might increase after a burst
324 of Ca^{2+} influx, due to the resulting release of paused retrograde trains. However, IFT
325 injection did not obviously increase after the returning IFT increased in this time range
326 (Figure 7B). Together, these results indicate that Ca^{2+} influx can restart paused IFT trains
327 and increase the amount of returning IFT trains to the base of flagella, but that IFT
328 injection is not controlled by Ca^{2+} influx and is not triggered by a transient increase in
329 arrival of retrograde trains.

Discussion

The role of Ca^{2+} dependent phosphorylation in IFT

The work of Liang et al. (2014) has clearly shown that the IFT kinesin is regulated by a calcium-dependent protein kinase (CDPK1). Why then in our hands do we not observe the expected effect of calcium channel modulation and Ca^{2+} depletion on length? For one thing, it has not been shown directly that this kinase requires Ca^{2+} for its activity in *Chlamydomonas*. Furthermore, it is important to note that regulation does not have to imply feedback control. Although we modeled the phosphorylation of kinesin as occurring in response to Ca^{2+} entering through the flagellar membrane, consistent with the original ion channel model (Rosenbaum, 2003), it is also possible that the phosphorylation is regulated by cytoplasmic Ca^{2+} fluctuations, which could be independent of the flagellum, thus constituting a separate regulatory input, but one that is not part of a feedback loop because it is not sensitive to flagellar length. This case may therefore be similar to the length-regulating kinase LF4 in *Chlamydomonas*. Null mutants in *lf4* have flagella that are approximately double normal length, but their length is still regulated in the sense that length variation is constrained (Bauer et al., 2021). Since length is still regulated in a null mutant of *lf4*, the kinase cannot be part of a feedback loop essential for length control. Instead, it is likely to carry information from other signaling pathways to alter the set-point of flagellar length. We speculate that the calcium-dependent regulation of kinesin entry into flagella during IFT may provide a way for cellular state, such as cell cycle or metabolic state, to influence flagellar length, and not as a feedback control loop necessary for length regulation *per se*. Liang and Pan (2013) also showed that another calcium-dependent protein kinase, CDPK3, helps flagellar assembly at low Ca^{2+} concentration. CDPK1 and CDPK3 may have opposite regulation over length control downstream of Ca^{2+}. We speculate that regulation of some flagella related process by cytoplasmic, rather than flagellar, calcium, may explain the long-known result that reduction in calcium leads to shortening or loss of flagella (Lefebvre et al., 1978) which has always stood in contradiction to the ion current model.

360 **The role of flagellar Ca^{2+} influx in flagellar length control**

361 The ion-current model assumed that the Ca^{2+} influx was stable. However, the amount of
362 Ca^{2+} influx was highly dispersed around the trend line although on average it is correlated
363 with flagellar length. This variability came from mostly the randomness of the Ca^{2+} influx
364 events. However, the Ca^{2+} influx events did not match a Poisson distribution, consistent
365 with the idea of Ca^{2+} bursting. Ca^{2+} influx may itself be regulated by some other process.
366 A previous study found that increased Ca^{2+} influx is evoked in the trailing flagellum during
367 gliding motility (Collingridge et al., 2013), and because our cells are also mounted on
368 surfaces, this could also be one source of variation in our experiments. The same group
369 also found that poly-lysine-coated coverslips can increase Ca^{2+} influx events in flagella
370 (Fort et al., 2021). These findings suggested that a mechanical stimulus on the flagellum
371 is one of the triggers of Ca^{2+} influx. The difference in Ca^{2+} influx between the two flagella
372 might also be related to the phototactic behavior of *Chlamydomonas*. To turn towards the
373 light source, *Chlamydomonas* cells can change beat frequency and beat pattern of each
374 flagellum (Rüffer and Nultsch, 1991), and they are controlled by Ca^{2+} (Kamiya and
375 Witman, 1984). This phototactic response is mediated by the signal transduction from the
376 photoreceptor, which is located at the eyespot (Harz and Hegemann, 1991). Because
377 these kinds of Ca^{2+} response are dependent on the specific local environment in which
378 the cell might find itself, it is unlikely to produce a stable signal, making it less useful as
379 an indicator of flagellar length.

380 The flagellar regeneration kinetics of 1 mM EGTA treated cells (Figure 5A) were
381 similar to results reported in rapamycin treated *Chlamydomonas* cells. Rapamycin
382 treated cells also showed slower flagella regeneration kinetics, but the length of the
383 flagellum eventually reached its original length before deflagellation (Yuan et al., 2012).
384 Rapamycin inhibits the mTOR pathway (Wullschleger et al., 2006), and it is known that
385 intracellular Ca^{2+} is necessary for the activation of mTOR pathway (Gulati et al., 2008; Li
386 et al., 2016). The slow regeneration kinetics of EGTA treated cells might be caused by
387 the inhibition of the cytoplasmic mTOR pathway.

388 It has been proposed that not only IFT injection, but also cargo loading onto IFT
389 particles, is regulated as a function of flagellar length (Craft et al., 2015). Quantitative

390 studies show that some of the apparent length-dependence of cargo loading may result
391 from the fact that in longer flagella, IFT trains are shorter and thus have fewer tubulin
392 binding sites (Wemmer et al., 2020). Nevertheless, the question arises whether flagellar
393 Ca^{2+} could play a role in regulating tubulin binding to the IFT particles. If this was the
394 case, Ca^{2+} would have to inhibit cargo binding, in order for cargo binding to decrease at
395 longer lengths as has been reported. Reduction of flagellar calcium should thus lead to
396 increased cargo binding, causing flagella to grow faster and/or to longer lengths. Our
397 measurements of flagellar growth rate (Figure 5A) show that in fact the opposite is true.
398 Taken together, our experimental test of the ion-current model for flagella length
399 control appears to rule out an ion channel model based on Ca^{2+} influx into flagella. It is
400 formally possible that some other ion might serve as a length sensor, but thus far Ca^{2+} is
401 the only candidate ion for which a plausible mechanistic link to IFT regulation has been
402 reported.
403 We previously provided experimental evidence against two other potential length
404 control models - an "initial bolus" model (Ludington et al., 2015) in which IFT particles are
405 initially injected into a newly formed flagellum but then recycle without being able to leave,
406 as well as a "time-of-flight" model (Ishikawa and Marshall, 2017; Ludington et al., 2015)
407 in which IFT particles contain a molecular timer that tracks the time spent inside the
408 flagellum as a proxy for flagellar length. Here we rule out a calcium-based ion-current
409 model for length sensing as well. Of the models we have considered, the remaining model
410 for length-dependent IFT regulation is one based on diffusive return of the IFT kinesin
411 (Hendel et al., 2018). The experiments presented here do not address this diffusion-
412 based model, which is thus far the only model for which there is no opposing experimental
413 evidence.
414
415 **Return of re-activated retrograde trains**
416 When anterograde IFT trains reach the tip, they remodel into a different number of
417 retrograde trains (Chien et al., 2017). Much less is known about possible remodeling of
418 retrograde trains at the basal body in order to re-inject them. One possibility might be that

419 some of returning IFT particles are immediately packaged into anterograde trains and re-
420 injected back into the same flagellum (Wingfield et al., 2017).

421 We observed re-activation of large paused retrograde trains by Ca^{2+} spikes, which
422 has been reported to occur due to an ability of Ca^{2+} influx to break the link between IFT
423 and membrane proteins and thus restart paused retrograde IFT trains (Fort et al., 2021).
424 We note in addition that many cytoplasmic dynein cargo adaptors contain EF hand
425 domains (Reck-Peterson et al., 2018), and at least in the case of CRACR2a it has been
426 shown that increased cellular calcium can activate dynein motility (Wang et al., 2019).
427 Regardless of the mechanism, the re-activation of these paused trains results in the
428 sudden return of a large quantity of IFT particles to the base, as visualized by a strong
429 retrograde trace. However, when we then looked at the anterograde trains entering the
430 flagellum in a short time period after the return of these trains, no significant increase in
431 IFT injection was observed (Figure 7). This observation implies that returning IFT particles
432 are not directly re-injected. This may indicate that the remodeling/recycling of retrograde
433 IFT trains into anterograde IFT trains simply needs more time, or it might be because IFT
434 injection is controlled by some other process that determines the timing of new particle
435 injection, regardless of instantaneous retrograde return events.

436

437 **Materials and methods**
438

439 ***Chlamydomonas* strains and culture condition**

440 *Chlamydomonas reinhardtii* strains, wild-type 137c (CC-125), the *fla3-1* mutant
441 expressing KAP-GFP (CC-4296)(Mueller et al., 2005), the *fla10-1* mutant (CC-
442 1919)(Huang et al., 1977), and the *pf2-4* mutant (CC-4404)(Rupp and Porter, 2003) were
443 obtained from the Chlamydomonas Resource Center (University of Minnesota, St. Paul,
444 MN). The *ppr2* mutant strain was provided by Kenjiro Yoshimura (Fujiu et al., 2009;
445 Matsuda et al., 1998). The *ift54-2* mutant strain expressing mScarlet-IFT54 was provided
446 by Karl Lechtreck (Fort et al., 2021; Wingfield et al., 2017). Generation of *pf2-1* DRC4-
447 GCaMP has been described (Nievergelt et al., 2021). To confirm the presence of mutant
448 alleles by PCR. *pf2-1* DRC4-GCaMP was crossed with the *pf2-4* mutant. We crossed the
449 *pf2-4* DRC4-GCaMP strain with the *ppr2* strain to generate *ppr2 pf2-4* double mutant
450 strain expressing DRC4-GCaMP. We generated the *ppr2* mutant expressing KAP-GFP
451 by crossing the *ppr2* mutant with the KAP-GFP strain. For dual-channel imaging of Ca^{2+}
452 and IFT, we crossed the *pf2-4* DRC4-GCaMP strain with *ift54-2* mScarlet-IFT54 strain to
453 generate the *pf2-4 ift54-2* double mutant strain expressing both DRC4-GCaMP and
454 mScarlet-IFT54. For flagellar disassembly assays, the *fla10-1* mutant strain was crossed
455 with the *ppr2* strain to generate *fla10-1 ppr2* double mutant strain. *Chlamydomonas* cells
456 were grown in liquid Tris-acetate-phosphate (TAP) medium media (20 mM Tris HCl, 3.5
457 mM NH_4Cl, 0.2 mM $MgSO_4$, 0.17 mM $CaCl_2$, 1 mM K_3PO_4, and 1000× diluted Hutner's
458 trace elements, titrated to pH 7.0 with glacial acetic acid) (Harris et al., 2009) at room
459 temperature with constant aeration in light.
460

461 **Flagellar regeneration and disassembly assays**

462 Flagellar regeneration assays were performed in the same manner as previously
463 described (Ishikawa and Marshall, 2017). Briefly, media of *Chlamydomonas* cell culture
464 were adjusted to pH 4.5 with 0.5 M acetic acid and incubated for 1 min to amputate
465 flagella, and then the pH was returned to pH 7.0 with 0.5 M KOH. The pH shocked cells
466 were pelleted by a centrifuge and resuspended with fresh TAP media with or without 1

467 mM EGTA (free Ca^{2+} is 149.3 nM and 170 μM, respectively). For flagellar disassembly
468 assay, we used the *fla10* temperature-sensitive kinesin mutant. The *fla10* mutant and
469 *fla10 ppr2* double mutant cells were cultured with TAP media at room temperature for one
470 day and then 1 mM EGTA was added, after which the cultures were transferred to a 33ºC
471 incubator with continuous illumination. Cells were fixed with 2.5% glutaraldehyde before
472 and at time points after pH shock or temperature shift. Fixed cells were imaged by
473 differential interference contrast (DIC) microscopy using an inverted microscope
474 (AxioVert 200M, Zeiss, Jena, Germany) with an air objective (Plan Apo 40x/NA 0.75,
475 Zeiss) and a CCD camera (Axiocam MRm, Zeiss). The lengths of 20 biflagellated cells at
476 each time point and each sample were measured using ImageJ (NIH, Bethesda, MD).
477 We often observed the *fla10* mutant and *fla10 ppr2* double mutant cells with a single
478 flagellum after the temperature shift but measured only the cells with two flagella. We did
479 not observe any *fla10 ppr2* double mutant cells with two flagella at 300 min after the
480 temperature shift.
481
482 **Live-cell imaging**
483 All live-cell imaging was performed during regeneration of flagella. *Chlamydomonas*
484 flagella were amputated by the pH shock method as described above. #1 (22 x 22 mm)
485 coverslips were coated with 0.1% poly-L-lysine solution (Sigma, St. Louis, MO) for 10 min
486 and washed three times with deionized water. Culture of flagella-regenerating cells was
487 placed on a poly-L-lysine-coated coverslip for 3 min and removed most of media. Then,
488 the coverslip was mounted on glass slides with 2% agarose/TAP with or without 1 mM
489 EGTA and sealed with VALAP (1:1:1 Vaseline, lanolin, and paraffin). Images were
490 acquired on an inverted microscope (Eclipse Ti-E, Nikon, Tokyo, Japan) configured for
491 TIRF microscopy using an oil objective (Apo TIRF 100 ×/NA 1.49; Nikon), MLC400 laser
492 combiner with solid-state lasers of 405, 488, 561, and 647nm (Keysight, Santa Rosa, CA)
493 and an electron-multiplying CCD (EM-CCD; iXon Ultra 897, Andor, Belfast, UK) camera
494 controlled with Nikon Elements Software (v5.20.00 b1423). Image sequences were
495 continuously acquired using triggered acquisition using the 488 nm and/or 561 nm lasers
496 (4.0 mW and 1.6 mW, respectively) and single band-pass (ET525/50m and ET600/60m,

497 Chroma, Bellows Falls, VT) or dual band-pass emission filters (59012m, Chroma) with a
498 camera exposure of 50 ms and an EM gain of 300 used for both channels.
499
500 **Quantifying axonemal DRC4-GCaMP**
501 To quantify the GCaMP reactivity, axonemes were isolated from the *pf2-4* DRC4-GCaMP
502 or *pf2-4* DRC4-mCherry-GCaMP strains. Flagellar isolation and demembranation were
503 performed as previously described (Wakabayashi and Kamiya, 2015). For Ca^{2+} titrations,
504 GCaMP axonemes were washed and resuspended with 30 mM MOPS, pH 7.2, 100 mM
505 KCl with either 10 mM EGTA (zero free Ca^{2+}) or 10 mM CaEGTA (39 μM free Ca^{2+}) from
506 the calcium calibration buffer kit (Thermo Fisher, Waltham, MA) and then observed on
507 the TIRF microscope (Eclipse Ti-E, Nikon). GCaMP intensity was measured using
508 ImageJ. Each axoneme was traced by hand using the Segmented line tool with 7-pixel
509 line width, analyzed by the Plot Profile function, and then calculated average intensity for
510 pixel. At least 13 axonemes were analyzed on each calcium concentration.
511
512 **Imaging analysis**
513 For GCaMP intensity analysis, kymographs were generated from movies of DRC4-
514 GCaMP using ImageJ. GCaMP kymographs were analyzed on MATLAB (MathWorks,
515 Natick, MA). The kymographs were smoothed using a 2D Gaussian filter and adjusted
516 intensity to minimize the effect of photobleaching. The peak of Ca^{2+} influx was detected
517 using the findpeaks function on MATLAB. The intensity of Ca^{2+} influx was calculated as
518 the sum of the peak area of Ca^{2+} influx divided by imaging time.
519 For quantitative analysis of IFT injection and behavior, kymographs were
520 generated from movies of KAP-GFP or mScarlet-IFT54 using Kymograph Clear (Mangeol
521 et al., 2016). IFT trajectories were detected using KymoButler, a deep learning-based
522 software (Jakobs et al., 2019), and extracted as coordinates. IFT kymographs and
523 coordinates of IFT trajectories were analyzed on MATLAB. IFT trajectories were
524 connected gaps and removed overlaps. The IFT intensity was calculated as the total
525 intensity of IFT trajectories per unit length and unit time. IFT velocity and frequency were
526 calculated from extracted IFT trajectories. The intensities of IFT injection and returning

527 IFT were calculated as the sum of average intensity of injecting or returning IFT
528 trajectories during the image of time.
529 For analysis of dual-channel imaging, dual-channel movies were converted to
530 kymographs by channel. The mScarlet channel showed slight bleed-through to the
531 GCaMP channel because we used the dual band-pass emission filter for imaging. To
532 remove the weak bleed-through mScaret-IFT54 signals from DRC4-GCaMP
533 kymographs, 20% intensity of the mScaret-IFT54 kymograph was subtracted from the
534 GCaMP kymograph. The intensity of Ca^{2+} influx was calculated in the same manner as
535 described above. To investigate the short-term effect of Ca^{2+} influx on IFT, we selected
536 the kymographs without Ca^{2+} influx for more than 10 s before the bundle of Ca^{2+} influx
537 that has more than 2,000 intensities. We calculated IFT injection, velocity, and frequency
538 for 10 s and 15 s each before and after the start of the Ca^{2+} influx in these kymographs.
539 The intensities of IFT injection and returning IFT were calculated as the sum of the
540 intensity of IFT trajectories that started from or returned to the base within the time range.
541 We also calculated the background intensity from the kymographs which removed both
542 anterograde and retrograde IFT trajectories. All calculations were performed using
543 custom-written routines in MATLAB.
544 For statistical analyses and graph generation, we used GraphPad Prism
545 (GraphPad, San Diego, CA). Statistical significance of Ca^{2+} influx between control and
546 the *ppr2* mutant was tested using unpaired t test. Statistical significances of IFT behaviors
547 were tested using paired t test.
548
549 **Computational model**
550 We constructed a computational model of flagellar length control based on the general
551 concept proposed by Rosenbaum (2003) and based on the biochemical work of Liang et
552 al on CDPK1 mediated phosphorylated of kinesin-2 (Liang et al., 2014). This model is
553 based on the following assumptions. First, as first proposed by Rosenbaum (Rosenbaum,
554 2003) based on the measurements of Beck and Uhl (Beck and Uhl, 1994), we assume
555 that the quantity of calcium entering the flagellum per unit time is on average proportional
556 to the length of the flagellum. Second, we assume that CDPK1 activity depends on the

557 instantaneous calcium concentration according to a saturable binding relation with some
558 dissociation constant that is an adjustable parameter of the model. In effect, this
559 assumption means that the kinetics of allosteric regulation of CDPK1 activity by calcium
560 occur on a much faster time scale than the other events of our model. Third, we assume
561 that phosphorylation of kinesin by CDPK1, as well as subsequent dephosphorylation of
562 kinesin, both take place on a fast timescale relative to the timescale of flagellar length
563 change, such that the fraction of active kinesin is at a quasi-state in the model. Given this
564 assumption, we represent the fraction of phosphorylated kinesin as a function of the
565 relative activity of CDPK1 according to a Michaelis-Menten equation. Fourth, based on
566 the results of Liang et al (Liang et al., 2014), we assume that the number of IFT particles
567 entering the flagellum per unit time is proportional to the fraction of non-phosphorylated
568 kinesin-2 proteins. Fifth, we assume that the occupancy of IFT particles for tubulin is
569 proportional to the quantity of tubulin available in the cytoplasm, which is equivalent to
570 saying that binding is not saturated. This was the assumption used in previous models
571 (Marshall et al., 2005) and is consistent with observations on the factional occupancy of
572 tubulin during flagellar assembly (Craft et al., 2015; Wemmer et al., 2020).
573 With these assumptions, we iteratively compute the net flagellar growth rate as the
574 difference between an assembly term and a disassembly term, where the disassembly
575 term is a length-independent constant (Marshall et al., 2005). The assembly term is
576 proportional to the size of the unused precursor pool (P-2L) where P is the total precursor
577 (tubulin) pool and L is the length of each of the two flagella as well as to the fraction of
578 non-phosphorylated kinesins. The net growth rate is used to update the length using the
579 Euler method with a timestep of 0.02 seconds. Output values are stored every 50
580 timesteps (1 second of simulation). Source codes of the model and data analyses used
581 in this work can be found here: https://github.com/ishikawaUCSF/temp
582

583 **Acknowledgements**

584

585 The authors thank current and past members of the Marshall laboratory as well as Joel
586 Rosenbaum and Xin Xiang for helpful discussions; DeLaine Larsen, Kari Herrington,
587 SoYeon Kim and the Nikon Imaging Center at UCSF for microscopy resources and
588 assistance; and Karl Lechtreck (University of Georgia) and Kenjiro Yoshimura (Shibaura
589 Institute of Technology) for generously sharing *Chlamydomonas* strains. This work was
590 supported by NIH grants R35GM130327 (W.F.M.) and R01GM130908 (M.D).

591

592

593 **Abbreviations**

594 CDPK: calcium-dependent protein kinase
595 DIC: differential interference contrast
596 DRC: dynein regulatory complex
597 GFP: green fluorescent protein
598 IFT: intraflagellar transport
599 KAP: kinesin-associated protein
600 TIRF: total internal reflection fluorescence

601

602 **References**

603

604 Bauer D, Ishikawa H, Wemmer KA, Hendel NL, Kondev J, Marshall WF. 2021. Analysis
605 of biological noise in the flagellar length control system. *iScience* **24**:102354.
606 doi:10.1016/j.isci.2021.102354

607 Beck C, Uhl R. 1994. On the localization of voltage-sensitive calcium channels in the
608 flagella of Chlamydomonas reinhardtii. *J Cell Biol* **125**:1119–1125.

609 Bottier M, Thomas KA, Dutcher SK, Bayly PV. 2019. How Does Cilium Length Affect
610 Beating? *Biophys J* **116**:1292–1304. doi:10.1016/j.bpj.2019.02.012

611 Chan Y-HM, Marshall WF. 2012. How cells know the size of their organelles. *Science*
612 **337**:1186–1189. doi:10.1126/science.1223539

613 Chien A, Shih SM, Bower R, Tritschler D, Porter ME, Yildiz A. 2017. Dynamics of the
614 IFT machinery at the ciliary tip. *eLife* **6**:e28606. doi:10.7554/eLife.28606

615 Collingridge P, Brownlee C, Wheeler GL. 2013. Compartmentalized calcium signaling in
616 cilia regulates intraflagellar transport. *Curr Biol* **23**:2311–2318.
617 doi:10.1016/j.cub.2013.09.059

618 Craft JM, Harris JA, Hyman S, Kner P, Lechtreck KF. 2015. Tubulin transport by IFT is
619 upregulated during ciliary growth by a cilium-autonomous mechanism. *J Cell Biol*
620 **208**:223–237. doi:10.1083/jcb.201409036

621 Engel BD, Ludington WB, Marshall WF. 2009. Intraflagellar transport particle size scales
622 inversely with flagellar length: revisiting the balance-point length control model. *J*
623 *Cell Biol* **187**:81–89. doi:10.1083/jcb.200812084

624 Engelke MF, Waas B, Kearns SE, Suber A, Boss A, Allen BL, Verhey KJ. 2019. Acute
625 inhibition of heterotrimeric kinesin-2 function reveals mechanisms of intraflagellar
626 transport in mammalian cilia. *Curr. Biol.* **29**:1137-1148. e4.
627 doi:10.1016/j.cub.2019.02.043

628 Fort C, Collingridge P, Brownlee C, Wheeler G. 2021. Ca2+ elevations disrupt
629 interactions between intraflagellar transport and the flagella membrane in
630 Chlamydomonas. *J Cell Sci* **134**:jcs253492. doi:10.1242/jcs.253492

631 Fujiu K, Nakayama Y, Iida H, Sokabe M, Yoshimura K. 2011. Mechanoreception in
632 motile flagella of Chlamydomonas. *Nat Cell Biol* **13**:630–632.
633 doi:10.1038/ncb2214
634 Fujiu K, Nakayama Y, Yanagisawa A, Sokabe M, Yoshimura K. 2009. Chlamydomonas
635 CAV2 encodes a voltage- dependent calcium channel required for the flagellar
636 waveform conversion. *Curr Biol* **19**:133–139. doi:10.1016/j.cub.2008.11.068
637 Gulati P, Gaspers LD, Dann SG, Joaquin M, Nobukuni T, Natt F, Kozma SC, Thomas
638 AP, Thomas G. 2008. Amino acids activate mTOR complex 1 via Ca2+/CaM
639 signaling to hVps34. *Cell Metab* **7**:456–465. doi:10.1016/j.cmet.2008.03.002
640 Harris EH, Stern DB, Witman GB, editors. 2009. Chapter 8 - Chlamydomonas in the
641 Laboratory The Chlamydomonas Sourcebook (Second Edition). London:
642 Academic Press. pp. 241–302. doi:10.1016/B978-0-12-370873-1.00008-3
643 Harz H, Hegemann P. 1991. Rhodopsin-regulated calcium currents in Chlamydomonas.
644 *Nature* **351**:489–491. doi:10.1038/351489a0
645 Hendel NL, Thomson M, Marshall WF. 2018. Diffusion as a Ruler: Modeling Kinesin
646 Diffusion as a Length Sensor for Intraflagellar Transport. *Biophys J* **114**:663–674.
647 doi:10.1016/j.bpj.2017.11.3784
648 Heuser T, Raytchev M, Krell J, Porter ME, Nicastro D. 2009. The dynein regulatory
649 complex is the nexin link and a major regulatory node in cilia and flagella. *J Cell*
650 *Biol* **187**:921–933. doi:10.1083/jcb.200908067
651 Huang B, Rifkin MR, Luck DJ. 1977. Temperature-sensitive mutations affecting flagellar
652 assembly and function in Chlamydomonas reinhardtii. *J Cell Biol* **72**:67–85.
653 Huang K, Diener DR, Mitchell A, Pazour GJ, Witman GB, Rosenbaum JL. 2007.
654 Function and dynamics of PKD2 in Chlamydomonas reinhardtii flagella. *J Cell*
655 *Biol* **179**:501–514. doi:10.1083/jcb.200704069
656 Ishikawa H, Marshall WF. 2017. Testing the time-of-flight model for flagellar length
657 sensing. *Mol Biol Cell* **28**:3447–3456. doi:10.1091/mbc.E17-06-0384
658 Ishikawa H, Marshall WF. 2011. Ciliogenesis: building the cell's antenna. *Nat Rev Mol*
659 *Cell Biol* **12**:222–234. doi:10.1038/nrm3085

660 Ishikawa H, Tian JL, Yu JE, Marshall WF, Qin H. 2022. Biosynthesis of Linear Protein
661 Nanoarrays Using the Flagellar Axoneme. *ACS Synth Biol* **11**:1454–1465.
662 doi:10.1021/acssynbio.1c00439
663 Jakobs MA, Dimitracopoulos A, Franze K. 2019. KymoButler, a deep learning software
664 for automated kymograph analysis. *eLife* **8**:e42288. doi:10.7554/eLife.42288
665 Jiang YY, Maier W, Baumeister R, Minevich G, Joachimiak E, Wloga D, Ruan Z,
666 Kannan N, Bocarro S, Bahraini A, Vasudevan KK, Lechtreck K, Orias E, Gaertig
667 J. 2019. LF4/MOK and a CDK-related kinase regulate the number and length of
668 cilia in Tetrahymena. *PLoS Genet*. **15**:e1008099
669 doi:10.1371/journal.pgen.1008099
670 Jordan MA, Diener DR, Stepanek L, Pigino G. 2018. The cryo-EM structure of
671 intraflagellar transport trains reveals how dynein is inactivated to ensure
672 unidirectional anterograde movement in cilia. *Nat Cell Biol* **20**:1250–1255.
673 doi:10.1038/s41556-018-0213-1
674 Kamiya R, Witman GB. 1984. Submicromolar levels of calcium control the balance of
675 beating between the two flagella in demembranated models of Chlamydomonas.
676 *J Cell Biol* **98**:97–107. doi:10.1083/jcb.98.1.97
677 Kumari D, Ray K. 2022. Phosphoregulation of kinesins involved in long-range
678 intracellular transport. *Front Cell Dev Biol*. **10**:873164.
679 doi:10.3389/fcell.2022.873164
680 Lechtreck KF, Van De Weghe JC, Harris JA, Liu P. 2017. Protein transport in growing
681 and steady-state cilia. *Traffic* **18**:277–286. doi:10.1111/tra.12474
682 Lefebvre PA, Nordstrom SA, Moulder JE, Rosenbaum JL. 1978. Flagellar elongation
683 and shortening in Chlamydomonas. IV. Effects of flagellar detachment,
684 regeneration, and resorption on the induction of flagellar protein synthesis. *J Cell*
685 *Biol* **78**:8–27. doi:10.1083/jcb.78.1.8
686 Li R-J, Xu J, Fu C, Zhang J, Zheng YG, Jia H, Liu JO. 2016. Regulation of mTORC1 by
687 lysosomal calcium and calmodulin. *eLife* **5**:e19360. doi:10.7554/eLife.19360

688 Liang Y, Pan J. 2013. Regulation of flagellar biogenesis by a calcium dependent protein
689 kinase in Chlamydomonas reinhardtii. *PloS One* **8**:e69902.
690 doi:10.1371/journal.pone.0069902
691 Liang Y, Pang Y, Wu Q, Hu Z, Han X, Xu Y, Deng H, Pan J. 2014. FLA8/KIF3B
692 phosphorylation regulates kinesin-II interaction with IFT-B to control IFT entry
693 and turnaround. *Dev Cell* **30**:585–597. doi:10.1016/j.devcel.2014.07.019
694 Liang Y, Zhu X, Wu Q, Pan J. 2018. Ciliary Length Sensing Regulates IFT Entry via
695 Changes in FLA8/KIF3B Phosphorylation to Control Ciliary Assembly. *Curr Biol*
696 **28**:2429-2435.e3. doi:10.1016/j.cub.2018.05.069
697 Ludington WB, Ishikawa H, Serebrenik YV, Ritter A, Hernandez-Lopez RA,
698 Gunzenhauser J, Kannegaard E, Marshall WF. 2015. A systematic comparison
699 of mathematical models for inherent measurement of ciliary length: how a cell
700 can measure length and volume. *Biophys J* **108**:1361–1379.
701 doi:10.1016/j.bpj.2014.12.051
702 Ludington WB, Wemmer KA, Lechtreck KF, Witman GB, Marshall WF. 2013.
703 Avalanche-like behavior in ciliary import. *Proc Natl Acad Sci U S A* **110**:3925–
704 3930. doi:10.1073/pnas.1217354110
705 Mangeol P, Prevo B, Peterman EJG. 2016. KymographClear and KymographDirect: two
706 tools for the automated quantitative analysis of molecular and cellular dynamics
707 using kymographs. *Mol Biol Cell* **27**:1948–1957. doi:10.1091/mbc.E15-06-0404
708 Marshall WF, Qin H, Rodrigo Brenni M, Rosenbaum JL. 2005. Flagellar length control
709 system: testing a simple model based on intraflagellar transport and turnover.
710 *Mol Biol Cell* **16**:270–278. doi:10.1091/mbc.E04-07-0586
711 Matsuda A, Yoshimura K, Sineshchekov OA, Hirono M, Kamiya R. 1998. Isolation and
712 characterization of novel Chlamydomonas mutants that display phototaxis but not
713 photophobic response. *Cell Motil Cytoskeleton* **41**:353–362.
714 doi:10.1002/(SICI)1097-0169(1998)41:4<353::AID-CM7>3.0.CO;2-0
715 Mueller J, Perrone CA, Bower R, Cole DG, Porter ME. 2005. The FLA3 KAP subunit is
716 required for localization of kinesin-2 to the site of flagellar assembly and

717 processive anterograde intraflagellar transport. *Mol Biol Cell* **16**:1341–1354.
718 doi:10.1091/mbc.E04-10-0931
719 Nakai J, Ohkura M, Imoto K. 2001. A high signal-to-noise Ca(2+) probe composed of a
720 single green fluorescent protein. *Nat Biotechnol* **19**:137–141. doi:10.1038/84397
721 Nievergelt AP, Zykov I, Diener D, Buchholz T-O, Delling M, Diez S, Jug F, Stěpánek L,
722 Pigino G. 2021. Intraflagellar transport trains can turn around without the ciliary
723 tip complex. doi:10.1101/2021.03.19.436138
724 Pazour GJ, Agrin N, Leszyk J, Witman GB. 2005. Proteomic analysis of a eukaryotic
725 cilium. *J Cell Biol* **170**:103–113. doi:10.1083/jcb.200504008
726 Pigino G, Geimer S, Lanzavecchia S, Paccagnini E, Cantele F, Diener DR, Rosenbaum
727 JL, Lupetti P. 2009. Electron-tomographic analysis of intraflagellar transport
728 particle trains in situ. *J Cell Biol* **187**:135–148. doi:10.1083/jcb.200905103
729 Quader H, Cherniack J, Filner P. 1978. Participation of calcium in flagellar shortening
730 and regeneration in Chlamydomonas reinhardii. *Exp Cell Res* **113**:295–301.
731 Reck-Peterson SL, Redwine WB, Vale RD, Carter AP. 2018. The cytoplasmic dynein
732 transport machinery and its many cargoes. *Nat Rev Mol Cell Biol* **19**:382–398.
733 doi:10.1038/s41580-018-0004-3
734 Reiter JF, Leroux MR. 2017. Genes and molecular pathways underpinning ciliopathies.
735 *Nat Rev Mol Cell Biol* **18**:533–547. doi:10.1038/nrm.2017.60
736 Rosenbaum J. 2003. Organelle size regulation: length matters. *Curr Biol* **13**:R506-507.
737 Rosenbaum JL, Moulder JE, Ringo DL. 1969. Flagellar elongation and shortening in
738 Chlamydomonas. The use of cycloheximide and colchicine to study the synthesis
739 and assembly of flagellar proteins. *J Cell Biol* **41**:600–619.
740 Rosenbaum JL, Witman GB. 2002. Intraflagellar transport. *Nat Rev Mol Cell Biol* **3**:813–
741 825. doi:10.1038/nrm952
742 Rüffer U, Nultsch W. 1991. Flagellar photoresponses of Chlamydomonas cells held on
743 micropipettes: II. Change in flagellar beat pattern. *Cell Motil Cytoskeleton*
744 **18**:269–278. doi:10.1002/cm.970180404

745 Rupp G, Porter ME. 2003. A subunit of the dynein regulatory complex in
746 Chlamydomonas is a homologue of a growth arrest-specific gene product. *J Cell*
747 *Biol* **162**:47–57. doi:10.1083/jcb.200303019
748 Tuxhorn J, Daise T, Dentler WL. 1998. Regulation of flagellar length in
749 Chlamydomonas. *Cell Motil Cytoskeleton* **40**:133–146. doi:10.1002/(SICI)1097-
750 0169(1998)40:2<133::AID-CM3>3.0.CO;2-G
751 Wakabayashi K, Kamiya R. 2015. Axonemal motility in Chlamydomonas. *Methods Cell*
752 *Biol* **127**:387–402. doi:10.1016/bs.mcb.2014.12.002
753 Wang Y, Huynh W, Skokan TD, Lu W, Weiss A, Vale RD. 2019. CRACR2a is a calcium-
754 activated dynein adaptor protein that regulates endocytic traffic. *J Cell Biol*
755 **218**:1619–1633. doi:10.1083/jcb.201806097
756 Wemmer K, Ludington W, Marshall WF. 2020. Testing the role of intraflagellar transport
757 in flagellar length control using length-altering mutants of Chlamydomonas.
758 *Philos Trans R Soc Lond B Biol Sci* **375**:20190159. doi:10.1098/rstb.2019.0159
759 Wingfield JL, Mengoni I, Bomberger H, Jiang Y-Y, Walsh JD, Brown JM, Picariello T,
760 Cochran DA, Zhu B, Pan J, Eggenschwiler J, Gaertig J, Witman GB, Kner P,
761 Lechtreck K. 2017. IFT trains in different stages of assembly queue at the ciliary
762 base for consecutive release into the cilium. *eLife* **6**:e26609.
763 doi:10.7554/eLife.26609
764 Wullschleger S, Loewith R, Hall MN. 2006. TOR signaling in growth and metabolism.
765 *Cell* **124**:471–484. doi:10.1016/j.cell.2006.01.016
766 Yuan S, Li J, Diener DR, Choma MA, Rosenbaum JL, Sun Z. 2012. Target-of-
767 rapamycin complex 1 (Torc1) signaling modulates cilia size and function through
768 protein synthesis regulation. *Proc Natl Acad Sci U S A* **109**:2021–2026.
769 doi:10.1073/pnas.1112834109
770

771 **Figure legends**

772

773 **Figure 1** Schematic diagram and modeling of the ion-current model.
774 (A) The ion-current model assumes the ion channels are uniformly distributed along the
775 length of flagella and ions entering the flagellum are proportional to the flagellar length.
776 Flagellar Ca^{2+} negatively regulates IFT injection into flagella to control the flagellar length.
777 The longer flagellum can intake more ions into flagella and these ions inhibits IFT injection
778 such that the further assembly of flagella is suppressed. (B) The schema of kinesin-2
779 inactivation by Ca^{2+} and CDPK1 based on Liang et al. (2014). In a Ca^{2+}-dependent
780 manner, CDPK1 phosphorylates FLA8, a subunit of heterotrimeric kinesin-2.
781 Phosphorylated kinesin-2 loses the activity to bind IFT proteins. (C, D) Simulated result
782 of the ion-current model based on kinesin-2 phosphorylation by CDPK1 (Liang et al.,
783 2014), as detailed in Materials and methods. Flagellar length (C) and the ratio of
784 phosphorylated kinesin (D) were plotted against time.

785

786 **Figure 2** DRC4-GCaMP quantitatively detects free Ca^{2+}.
787 (A) DIC and fluorescent images of DRC4-GCaMP cells. DRC4-GCaMP localizes to the
788 entire length of flagella. Scale bar: 10 μm. (B) Fluorescent images of isolated DRC4-
789 mCherry-GCaMP axonemes. Axonemes were isolated from DRC4-mCherry-GCaMP
790 cells and were treated with various concentration of free Ca^{2+}. GCaMP intensity was
791 increased as free Ca^{2+} concentration increased. Scale bar: 10 μm. (C) Semilogarithmic
792 plot of GCaMP and mCherry intensities. GCaMP and mCherry intensities were measured
793 and plotted. The blue dashed line shows equation of sigmoidal curve which is calculated
794 from data.

795

796 **Figure 3** Quantification of Ca2+ influx as a function of flagellar length.
797 (A) Representative DRC4-GCaMP kymographs of *Chlamydomonas* flagella in control
798 (*pf2* DRC4-GCaMP), *ppr2* mutant (*pf2 ppr2* DRC4-GCaMP), and 1 mM EGTA treated
799 (*pf2* DRC4-GCaMP) cells. These kymographs were assembled from Movies S1-3.
800 Horizontal bar: 5 s; vertical bar: 5 μm. (B) The intensity of Ca^{2+} influx into flagella was

801 calculated from kymographs and plotted against flagellar length. Different length flagella
802 were obtained by imaging flagella during regeneration. Control (blue circles, n = 198,
803 Pearson correlation coefficient ρ = 0.33, and coefficient of determination r^2 = 0.11) and
804 the *ppr2* mutant (red squares, n = 182, ρ = 0.14, and r^2 = 0.02). (C) The frequency of Ca^{2+}
805 influx was plotted against flagellar length. No obvious correlation was detected in either
806 the control (blue circles, ρ = 0.14, and r^2 = 0.02) or the *ppr2* mutant cells (red squares, ρ
807 = 0.004, and r^2 = 0.00002). (D) A box-and-whisker plot shows the mean difference of Ca^{2+}
808 influx intensity from the control regression line. Significance was determined by an
809 unpaired two-tailed t test (*** $P < 0.001$).
810
811 **Figure 4** Quantification of IFT injection as a function of flagellar length.
812 (A) Representative KAP-GFP kymographs of *Chlamydomonas* flagella in control (*fla3*
813 KAP-GFP), *ppr2* mutant (*fla3 ppr2* KAP-GFP), and 1 mM EGTA treated (*fla3* KAP-GFP)
814 cells. These kymographs were assembled from Movies S4-6. Horizontal bar: 5 s; vertical
815 bar: 5 *μ*m. (B) The mean KAP-GFP intensity of each flagellum was calculated from
816 kymographs and plotted against flagellar length. Control (blue circles, n = 196, ρ = -0.73,
817 and r^2 = 0.54), *ppr2* (red squares, n = 192, ρ = -0.52, and r^2 = 0.27), and EGTA (orange
818 triangles, n = 162, ρ = -0.52, and r^2 = 0.28). (C) The frequency of KAP-GFP was plotted
819 against flagellar length. Control (blue circles, ρ = 0.09, and r^2 = 0.008), *ppr2* (red squares,
820 ρ = 0.51, and r^2 = 0.26), and EGTA (orange triangles, ρ = 0.14, and r^2 = 0.02). (D) The
821 velocity of KAP-GFP was plotted against flagellar length. Control (blue circles, ρ = 0.63,
822 and r^2 = 0.40), *ppr2* (red squares, ρ = 0.81, and r^2 = 0.64), and EGTA (orange triangles,
823 ρ = 0.69, and r^2 = 0.47).
824
825 **Figure 5** The kinetics of flagellar regeneration and disassembly.
826 (A) Flagella were removed by the pH shock method. Mean flagellar length of control (wild-
827 type CC-125, blue circles), *ppr2* mutant (red squares), 1 mM EGTA treated (orange
828 triangle), and 1 mM $CaCl_2$ treated (green diamonds) cells was plotted against time after
829 pH shock. (B) The *fla10* mutant strains were transferred to the restrictive temperature
830 (33°C). Mean flagellar length of control (*fla10*, blue circles), *fla10 ppr2* mutant (red

831 triangle), 1 mM EGTA treated *fla10* (orange diamonds), and 1 mM EGTA treated *fla10*
832 *ppr2* (magenta inverted triangles) cells was plotted against time after temperature shift.
833 20 biflagellated cells were measured per strain and time point.
834
835 **Figure 6** Dual-channel imaging of DRC4-GCaMP and mScarlet-IFT54.
836 (A) Representative kymographs and quantified data. The DRC4-GCaMP kymograph (top)
837 was generated from Movie S7. Quantified intensity of Ca^{2+} influx is shown at the bottom
838 of the kymograph. The mScarlet-IFT54 kymograph (middle) was generated from Movie
839 S7. Quantified anterograde IFT injection is shown at the bottom of the kymograph. The
840 merged kymograph (bottom) of DRC4-GCaMP (green) and mScarlet-IFT54 (magenta).
841 Horizontal bar: 5 s; vertical bar: 5 μm. (B) The mScarlet-IFT54 intensity of each flagellum
842 was calculated from kymographs and plotted against flagellar length (n = 116, and
843 Pearson correlation coefficient ρ = -0.47). Non-linear regression is indicated by a solid
844 line (r^2 = 0.21). (C) The frequency of anterograde IFT was plotted against flagellar length
845 (ρ = 0.53, and r^2 = 0.28). (D) The velocity of anterograde IFT was plotted against flagellar
846 length (ρ = 0.76, and r^2 = 0.58). (E) The intensity of Ca^{2+} influx into flagella was calculated
847 from kymographs and plotted against flagellar length (ρ = 0.33, and r^2 = 0.11). (F) The
848 mean mScarlet-IFT54 intensity was plotted against the intensity of Ca^{2+} influx (ρ = -0.08,
849 and r^2 = 0.007).
850
851 **Figure 7** Quantification of IFT behavior after Ca^{2+} influx.
852 (A) Overview of the short-time analysis of IFT behavior after a burst of Ca^{2+} influx using
853 dual-channel imaging. Analyzed areas were colored on the representative kymographs
854 of DRC4-GCaMP and mScarlet-IFT54. Intervals of each area are 5 s. Bursts of Ca^{2+}
855 influx in which a previous Ca^{2+} influx was observed at least 10 s before the Ca^{2+} influx
856 were selected. The “c” area was set at the start of the burst of Ca^{2+} influx. The areas “a”
857 and “b” were set to 10 s and 5 s before the burst of Ca^{2+} influx at the “c” area. The “c”
858 area was set at the start of the burst of Ca^{2+} influx. The areas “d” and “e” were set to 5 s
859 and 10 s after the start of the Ca^{2+} influx. Horizontal bar: 5 s; vertical bar: 5 μm. (B-G) IFT
860 behaviors before and after the burst of Ca^{2+} influx were plotted against each area (n =

861 29). (B) The intensity of IFT injection. (C) The intensity of returning IFT. (D) The frequency
862 of anterograde IFT. (E) The frequency of retrograde IFT. (F) The velocity of anterograde
863 IFT. (G) The velocity of anterograde IFT. (H) The sum of the Ca^{2+} influx before and after
864 the burst of Ca^{2+} influx. (I) The background intensity of mScarlet-IFT54. Significance
865 between each area was determined by paired t test (* $P < 0.05$, ** $P < 0.01$, *** $P < 0.001$
866 and **** $P < 0.0001$).
867
868
869 **Supporting Information**
870
871 **Figure S1**
872 Example DRC4-GCaMP kymographs of *Chlamydomonas* flagella (control, *pf2* DRC4-
873 GCaMP). The pair of Flagellum 1 and Flagellum 2 are flagella from the same cells. The
874 pattern of Ca^{2+} influx events varied from flagellum to flagellum and from time to time.
875 Horizontal bar: 5 s; vertical bar: 5 μm.
876
877 **Figure S2**
878 Individual Ca^{2+} influx events are not independent. Histogram of Ca^{2+} spikes distribution
879 every 5 s. Blue line shows the DRC4-GCaMP (control) data from Figure 3. Red dashed
880 line shows calculated data to fit with Poisson distribution. Blue line does not fit with red
881 line (Chi-square goodness-of-fit test, $p < 0.0001$). Similar results were obtained at other
882 time intervals.
883
884 **Movie S1**
885 Movie of DRC4-GCaMP in control (*fla3* KAP-GFP) cell. This movie was taken at 20
886 frames per second (fps) and plays in real time.
887
888 **Movie S2**
889 Movie of DRC4-GCaMP in the *ppr2* mutant (*fla3 ppr2* KAP-GFP) cell. This movie was
890 taken at 20 fps and plays in real time.

891

892 **Movie S3**

893 Movie of DRC4-GCaMP in 1 mM EGTA treated (*fla3* KAP-GFP) cell. This movie was
894 taken at 20 fps and plays in real time.

895

896 **Movie S4**

897 Movie of KAP-GFP in control (*fla3* KAP-GFP) cell. This movie was taken at 20 fps and
898 plays in real time.

899

900 **Movie S5**

901 Movie of KAP-GFP in the *ppr2* mutant (*fla3 ppr2* KAP-GFP) cell. This movie was taken at
902 20 fps and plays in real time.

903

904 **Movie S6**

905 Movie of KAP-GFP in 1 mM EGTA treated (*fla3* KAP-GFP) cell. This movie was taken at
906 20 fps and plays in real time.

907

908 **Movie S7**

909 Movie of DRC4-GCaMP and mScarlet-IFT54 in the *pf2 ift54* DRC4-GCaMP mScarlet-
910 IFT54 cell. DRC4-GCaMP is shown in green, and mScarlet-IFT54 is shown in magenta.
911 This movie was taken at 10 fps and plays in real time.

912

913

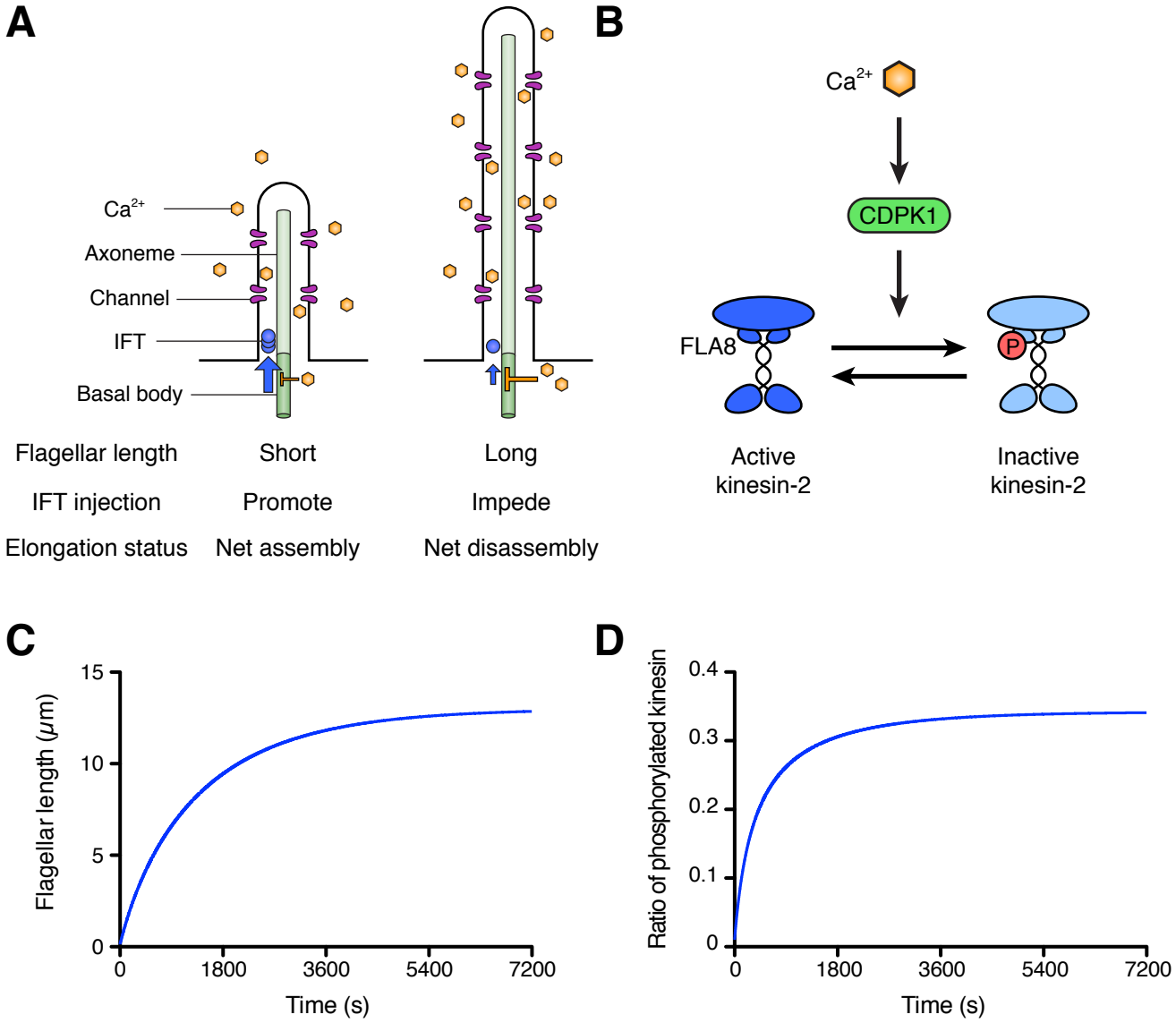
A
Ca2+
Axoneme
Channel
IFT
Basal body
Flagellar length
Short
Long
IFT injection
Promote
Impede
Elongation status
Net assembly
Net disassembly
B
Ca2+
CDPK1
FLA8
P
Active kinesin-2
Inactive kinesin-2
C
Flagellar length (μm)
15
10
5
0
0
1800
3600
5400
7200
Time (s)
D
Ratio of phosphorylated kinesin
0.4
0.3
0.2
0.1
0
0
1800
3600
5400
7200
Time (s)

Figure 1

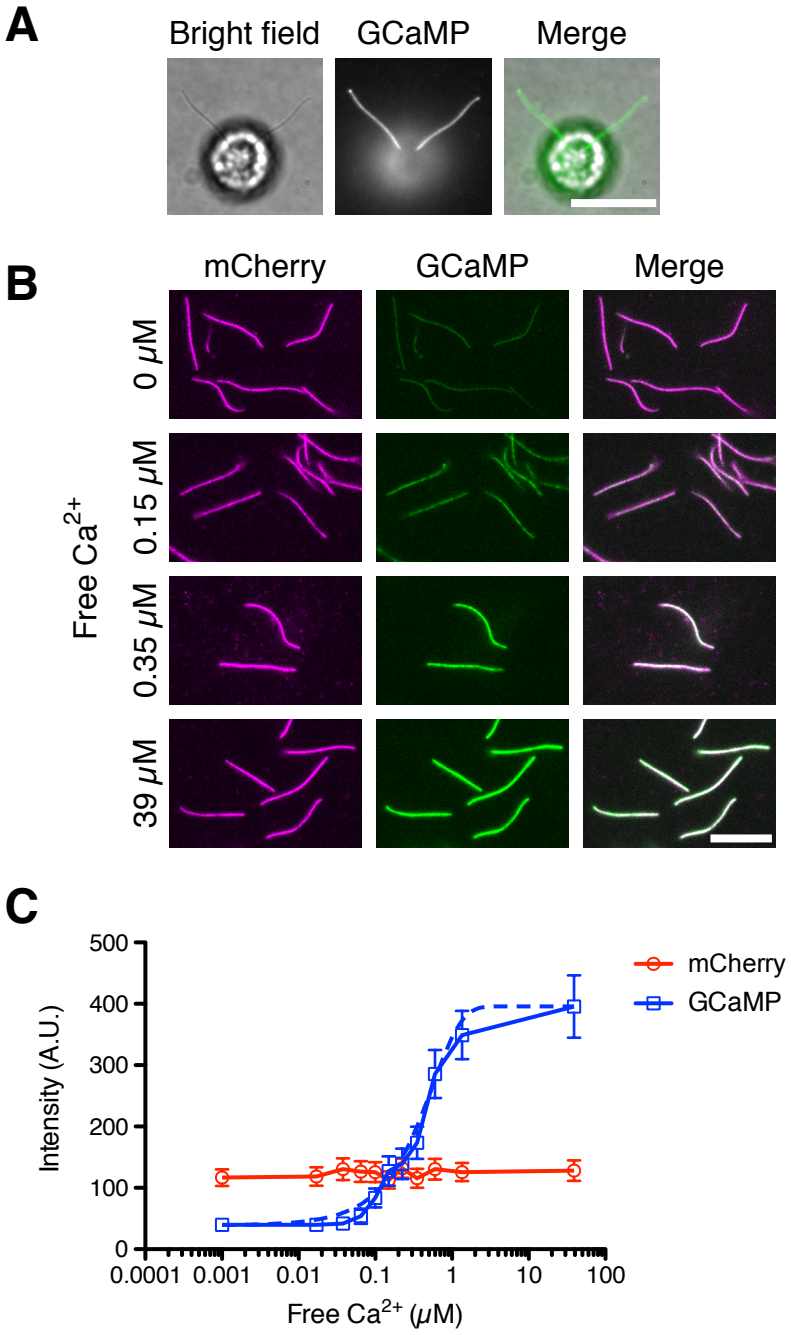
A
Bright field
GCaMP
Merge
B
mCherry
GCaMP
Merge
Free Ca2+
0 μM
0.15 μM
0.35 μM
39 μM
C
Intensity (A.U.)
500
400
300
200
100
0
0.0001
0.001
0.01
0.1
1
10
100
Free Ca2+ (μM)
mCherry
GCaMP

Figure 2

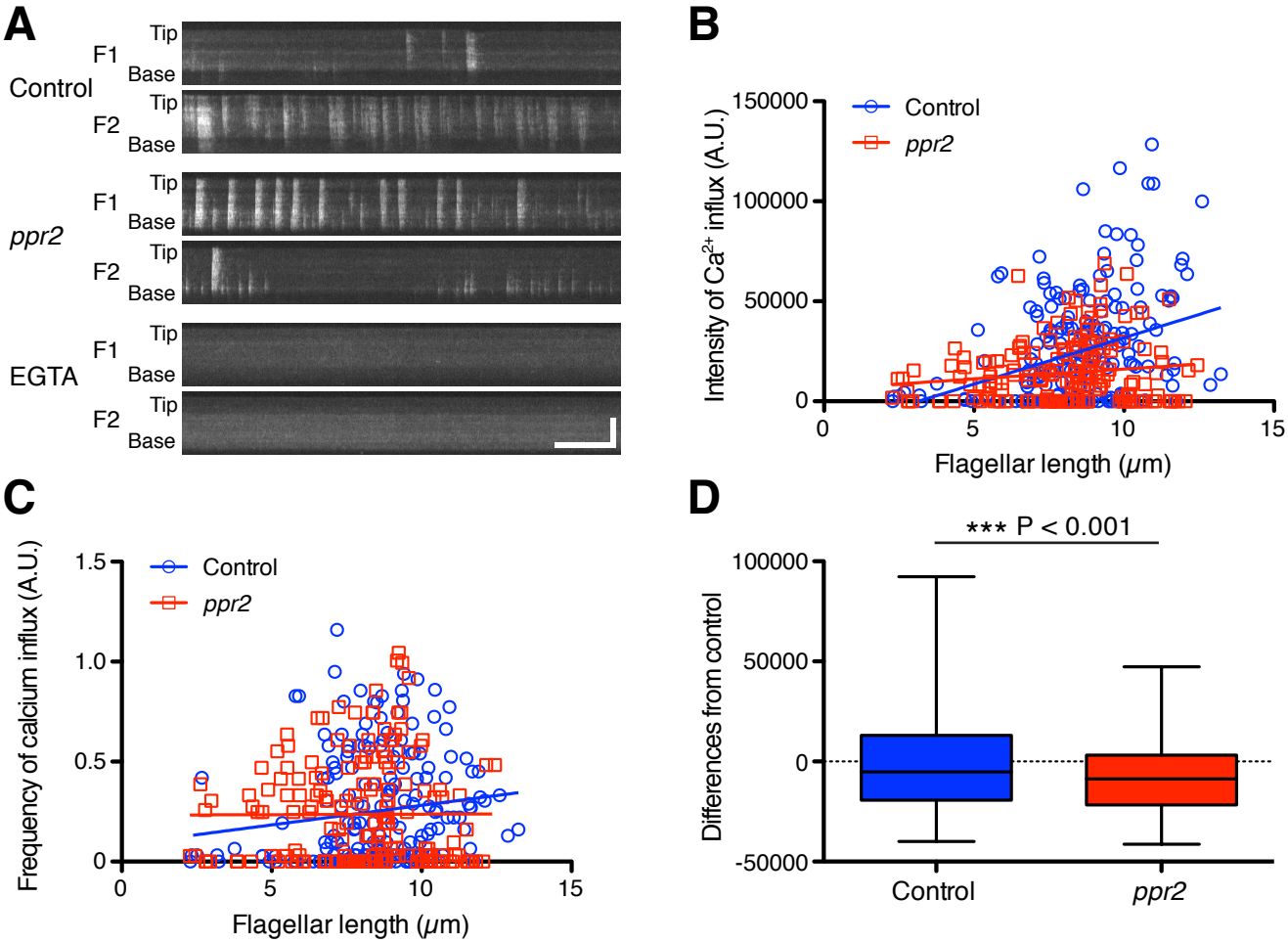
A
Control
F1
Tip
Base
F2
Tip
Base
ppr2
F1
Tip
Base
F2
Tip
Base
EGTA
F1
Tip
Base
F2
Tip
Base
B
Control
ppr2
Intensity of Ca2+ influx (A.U.)
150000
100000
50000
0
0
5
10
15
Flagellar length (μm)
C
Control
ppr2
Frequency of calcium influx (A.U.)
1.5
1.0
0.5
0
0
5
10
15
Flagellar length (μm)
D
*** P < 0.001
Differences from control
100000
50000
0
-50000
Control
ppr2

Figure 3

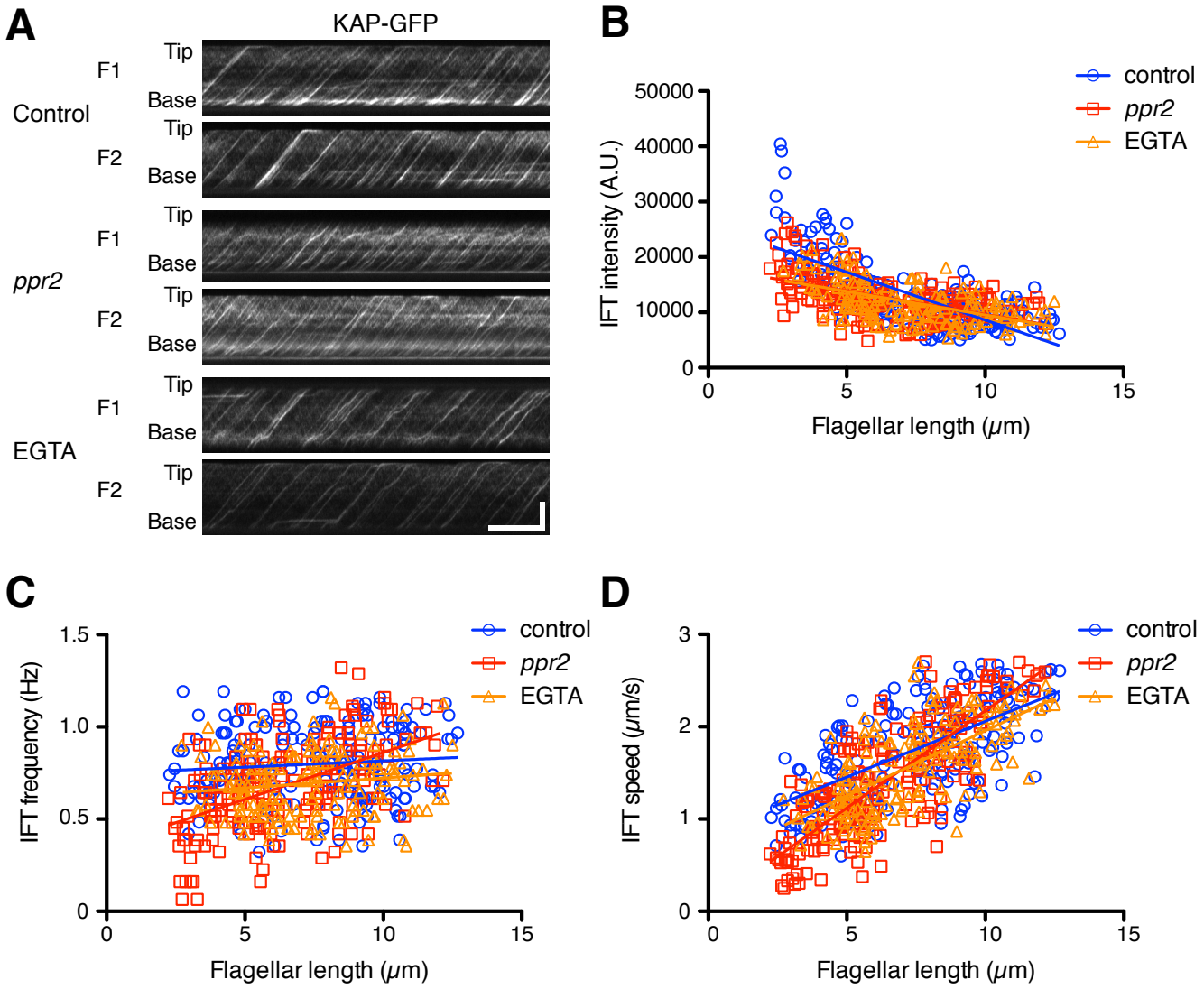
A
KAP-GFP
Control
F1
Tip
Base
F2
Tip
Base
ppr2
F1
Tip
Base
F2
Tip
Base
EGTA
F1
Tip
Base
F2
Tip
Base
B
control
ppr2
EGTA
IFT intensity (A.U.)
50000
40000
30000
20000
10000
0
0
5
10
15
Flagellar length (μm)
C
control
ppr2
EGTA
IFT frequency (Hz)
1.5
1.0
0.5
0
0
5
10
15
Flagellar length (μm)
D
control
ppr2
EGTA
IFT speed (μm/s)
3
2
1
0
0
5
10
15
Flagellar length (μm)

Figure 4

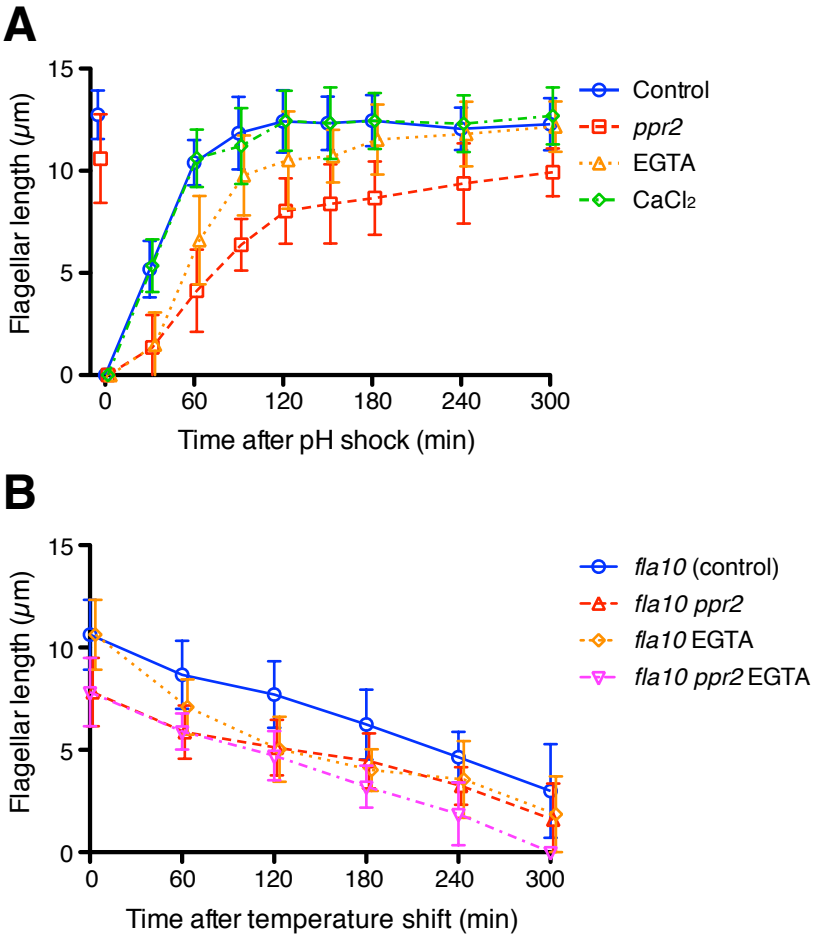
A
Flagellar length (μm)
15
10
5
0
0
60
120
180
240
300
Time after pH shock (min)
Control
ppr2
EGTA
CaCl2
B
Flagellar length (μm)
15
10
5
0
0
60
120
180
240
300
Time after temperature shift (min)
fla10 (control)
fla10 ppr2
fla10 EGTA
fla10 ppr2 EGTA

Figure 5

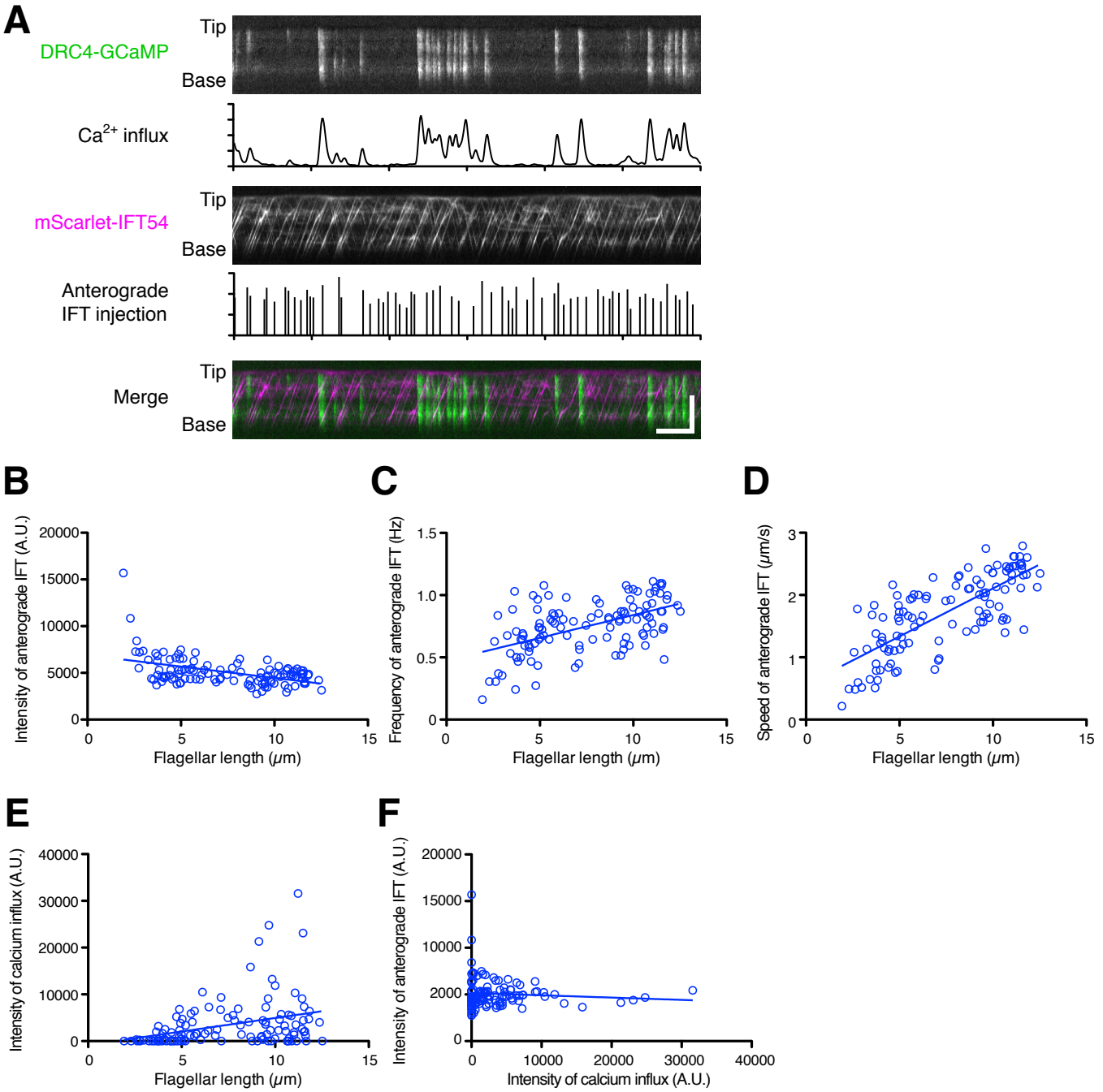
A
DRC4-GCaMP
Tip
Base
Ca2+ influx
mScarlet-IFT54
Tip
Base
Anterograde
IFT injection
Merge
Tip
Base
B
Intensity of anterograde IFT (A.U.)
Flagellar length (μm)
C
Frequency of anterograde IFT (Hz)
Flagellar length (μm)
D
Speed of anterograde IFT (μm/s)
Flagellar length (μm)
E
Intensity of calcium influx (A.U.)
Flagellar length (μm)
F
Intensity of anterograde IFT (A.U.)
Intensity of calcium influx (A.U.)

Figure 6

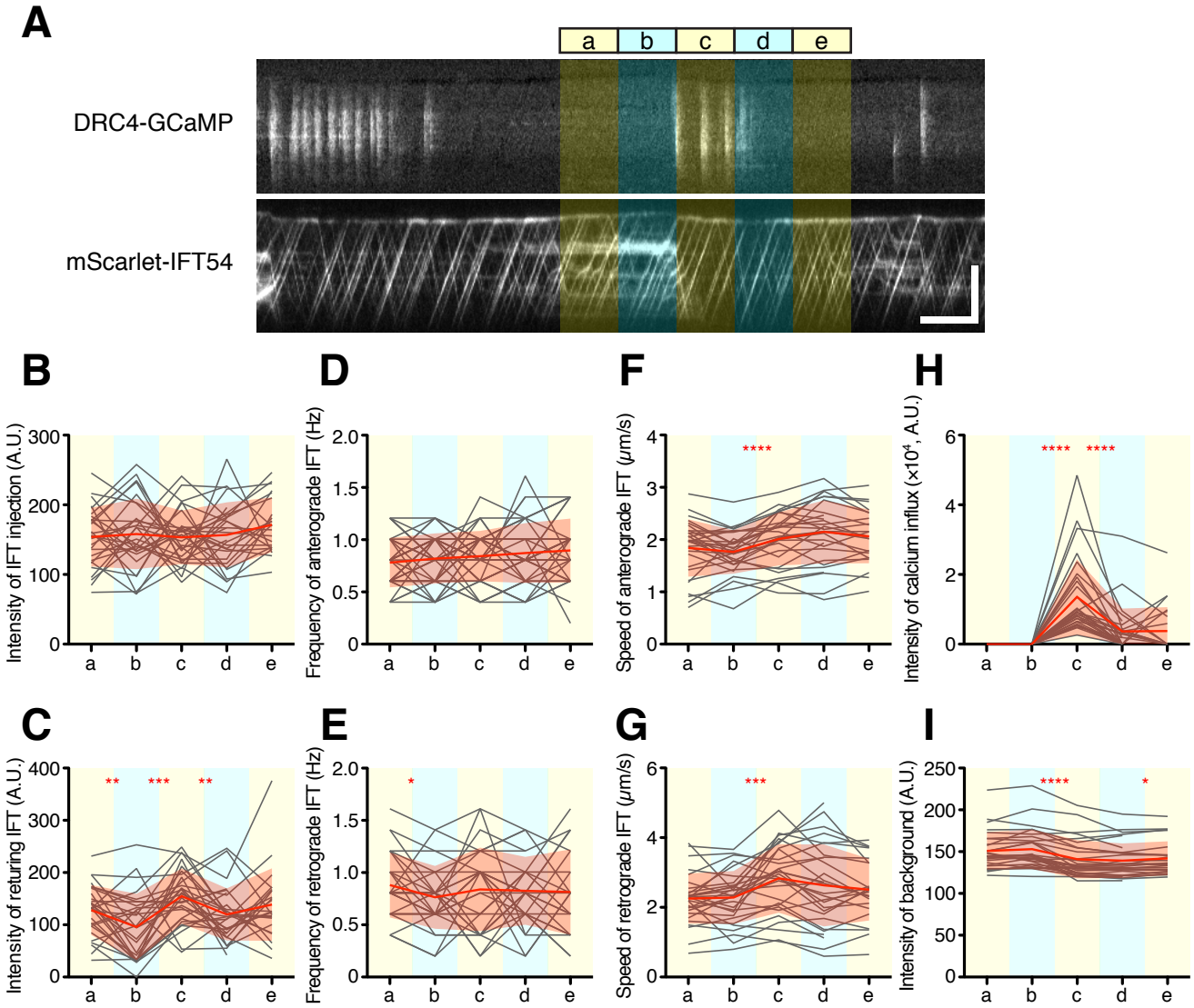
A
a
b
c
d
e
DRC4-GCaMP
mScarlet-IFT54
B
Intensity of IFT injection (A.U.)
C
Intensity of returing IFT (A.U.)
D
Frequency of anterograde IFT (Hz)
E
Frequency of retrograde IFT (Hz)
F
Speed of anterograde IFT (μm/s)
G
Speed of retrograde IFT (μm/s)
H
Intensity of calcium influx (x10⁴, A.U.)
I
Intensity of background (A.U.)

Figure 7

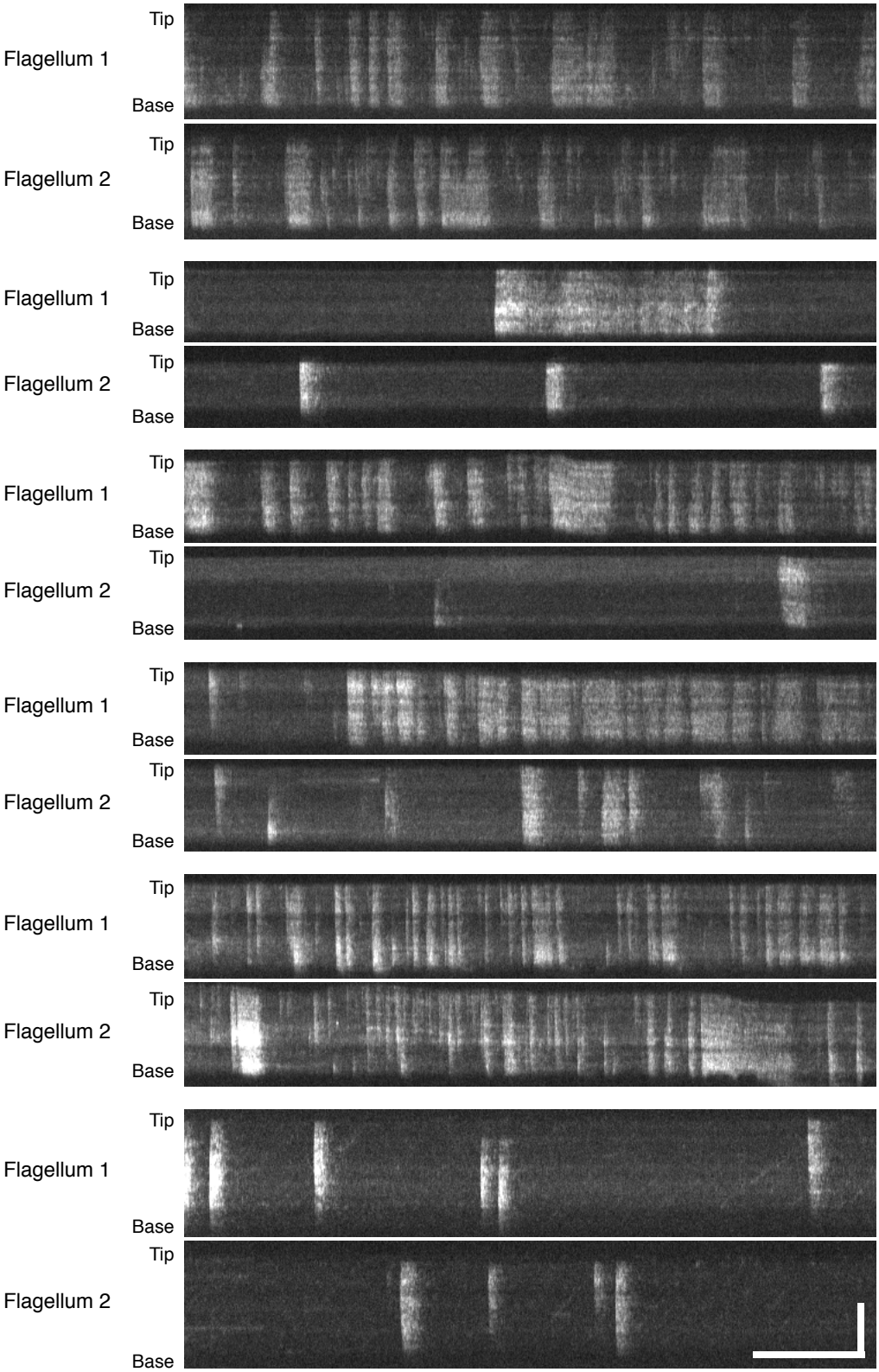
Flagellum 1
Tip
Base
Flagellum 2
Tip
Base
Flagellum 1
Tip
Base
Flagellum 2
Tip
Base
Flagellum 1
Tip
Base
Flagellum 2
Tip
Base
Flagellum 1
Tip
Base
Flagellum 2
Tip
Base
Flagellum 1
Tip
Base
Flagellum 2
Tip
Base

Figure S1

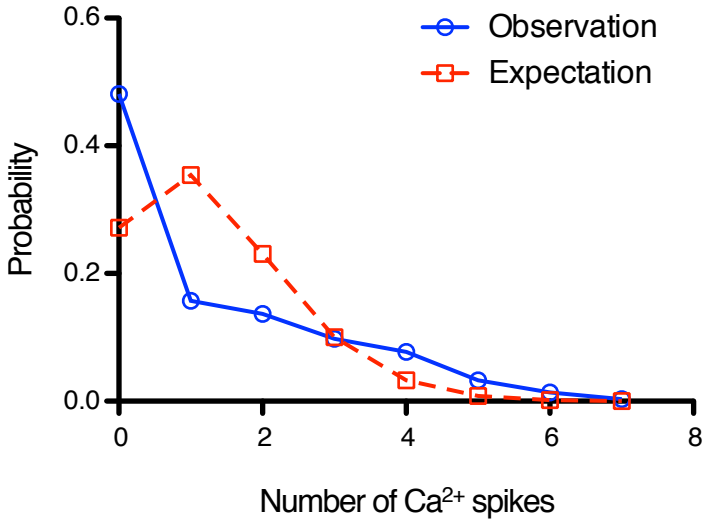
Observation
Expectation
Probability
0.6
0.4
0.2
0.0
0
2
4
6
8
Number of Ca2+ spikes

Figure S2